Supporting information for:

The Hydrated Electron at the Surface of Neat Liquid Water Appears to Be Indistinguishable from the Bulk Species

Marc P. Coons, Zhi-Qiang You, and John M. Herbert*

Department of Chemistry and Biochemistry, The Ohio State University, Columbus, OH 43210

E-mail: herbert@chemistry.ohio-state.edu

This document provides additional details of the simulations using one-electron models, the density functional theory (DFT) and second-order Møller-Plesset (MP2) calculations, and the non-equilibrium solvation models.

1 One-Electron Pseudopotential Simulations

This section describes the simulations that were used to produce Figs. 1 and 2, as well as the averages in Table 1. Additional trajectories were run to test convergence of the sampling procedure, and these tests are described in Section 1.3.

1.1 Pseudopotentials

The simulations of an excess electron in bulk liquid water and at the liquid water/vapor interface employed two different one-electron pseudopotential models. One of these, which we call the "mean-field polarization model", was developed by Turi and Borgis[S1] and is based upon the non-polarizable SPC water model,[S2] but includes a mean-field polarization potential $\propto r^{-4}$, where r is the electron–water distance. The other model, developed by Jacobson and Herbert,[S3] is built upon the polarizable AMOEBA water model[S4] and includes electron–water polarization explicitly and self-consistently. (Polarization is handled in AMOEBA by

*To whom correspondence should be addressed

means of atom-centered inducible dipoles, and the induced dipoles in turn interact with the wave function. Schrödinger's equation for the wave function is iterated to self-consistency alongside the equations for the induced dipoles.[S3,S5]) These models have been used in myriad previous hydrated electron simulations.[S1,S3,S6–S19] Both afford accurate optical spectra for e^-(aq) in bulk water,[S1,S3] and in addition the explicit polarization model performs well in reproducing MP2/6-31(1+,3+)G* benchmarks for $(H_2O)_N^-$ clusters (N = 2–33),[S3] including both relative isomer energies and vertical electron binding energies (VEBEs). In the latter case, the mean deviation between the VEBE predicted by the one-electron model and the MP2 benchmark is 0.041 eV for 95 unique cluster structures.[S3] With this level of accuracy, the explicit polarization model successfully accounts for trends observed in the gas-phase photoelectron spectra of $(H_2O)_N^-$ clusters.[S16]

1.2 Simulation Details

Initial structures were extracted from equilibrated neat liquid water simulations utilizing either the SPC or the AMOEBA water model, as appropriate. These simulations were performed with $N = 200$ water molecules in a periodic unit cell at $T = 300$ K, where the unit cell size was set such that the density is $\rho = 0.997$ g cm^{-3}. For a cubic cell, this would correspond to 18.1617 Å on a side, but to simulate the water/vacuum interface we set $L_x = L_y = 18.1617$ Å in the x and y directions, but $L_z = 5L_x$ in the z direction, thus creating a periodic "slab" of water that is ≈ 18 Å thick in the z direction and surrounded by vacuum out to $L_z = 90.8085$ Å. Standard three-dimensional Ewald summation is employed to sum the electrostatic interactions, so that the slab is actually periodically replicated in the z direction. If the slab of water has a non-zero dipole moment (which, in general, one should expect) then the potential energy must be corrected for the spurious electric fields that are produced from the dipolar interactions between periodically-replicated slabs. The appropriate correction is derived in Ref. S20 for the case of an infinitely thin slab, and it is noted in Ref. S21 that higher-order terms are required for a slab having finite thickness, unless the spacing between periodic images is three to five times larger than the slab thickness. For this reason we set $L_x = 5L_z$ and incorporate only the first-order dipolar correction to the Ewald sum.

The neat liquid water simulations described above were equilibrated for 100 ps, and starting structures for the e^-(aq) simulations were randomly chosen from the final 10 ps of the equilibration run. At $t = 0$, an electron is introduced into the system by turning on electron–water interactions using the appropriate pseudopotential. The electronic wave function is represented on a rectangular grid that spans the unit cell in the x and y directions and extends into vacuum in the z direction to a distance equal to the thickness of the slab (*i.e.*, the total span of the grid in the z direction equals twice the thickness of the slab). The grid spacing is $\Delta x = \Delta y = \Delta z = 0.95$ Å in all directions, as in previous work.[S3]

For consistency, both the bulk and the interfacial hydrated electron simulations use slab boundary conditions. We do this for two reasons: first, we wish to allow the possibility that an electron in bulk water might spontaneously migrate to the interface; and second, so that even for e^-(aq) in bulk water we can measure the distance d between the centroid of the electron's wave function and the Gibbs dividing surface (GDS), defined as the locus of points in the z direction where the solvent density has fallen to half its value in bulk

solution. This surface is computed on-the-fly at each point (x, y) and at each time step, and is used to demarcate the liquid/vacuum interface for the purpose of computing d. Our coordinate system sets $z = 0$ at the GDS; this is the coordinate labeled d in the text, so for a slab whose thickness is ≈ 18 Å, the center of the slab corresponds to $d \approx -9$ Å. This explains the locus of points near $d = -9$ Å in Fig. 3(b). Whereas trajectories for e^-(aq) at the water/vacuum interface are initialized from equilibrated neutral water, for which the electron naturally attaches at the interface, all of these trajectories eventually internalize and these equilibrated, internalized trajectories are then used as initial conditions for e^-(aq) in bulk water.

For each one-electron model, twenty independent trajectories for the interfacial species e^-(aq) were propagated at $T = 300$ K using a home-built simulation code, FURRY, that is described in detail in Ref. S5, and has been used extensively for this purpose in other work.[S3,S5,S13,S14,S16] Ewald summation is used for the e^-(aq) simulations in the same way that is described above for neutral liquid water, and a Nosé-Hoover thermostat is used to provide temperature control. The interfacial e^-(aq) simulations were propagated for 80 ps for the mean-field polarization model and for 40 ps in the case of the explicit polarization model in order to obtain statistics. The electron was determined to be internalized when the centroid of its wave function stabilizes around the center of the water slab ($d \approx -9$ Å), which occurs on a time scale no longer than 25–35 ps. Snapshots from one such trajectory are shown in Fig. 1. Following internalization, each trajectory was propagated for an additional 50 ps to examine whether the electron might return to the surface, but in no case was this observed and the internalized electron fluctuates no farther than 1.0–1.5 Å from the center of the water slab. Following this additional 50 ps of equilibration time, these trajectories were taken to be the initial ($t = 0$) conditions for the simulation of e^-(aq) in bulk water.

1.3 Convergence Tests

Additional testing was performed to examine the dependence of our results on the number of water molecules, choice of simulation grid and periodic unit cell, and initial conditions. To this end we performed twenty simulations each with $N = 300$ and $N = 600$ water molecules in the unit cell, using the mean-field Turi-Borgis polarization model at $T = 300$ K. The density was kept the same as the smaller simulations discussed above ($\rho = 0.997$ g cm^{-3}), which in the present cases means $L_x = L_y = 20.7961$ Å for $N = 300$ and $L_x = L_y = 26.2105$ Å for $N = 600$, with $L_z = 5L_x$ in all cases. The simulation grid representing the electronic wave function was chosen in the same manner as above, with $\Delta x = \Delta y = \Delta z = 0.95$ Å. To make the calculations tractable (because the dimension of the Hamiltonian is equal to the total number of grid points in three dimensions), we used the same simulation grid for $N = 600$ that we did for $N = 300$, so in the former case the grid does not extend quite to the edges of the simulation cell. (Since the electron localizes rapidly in each trajectory, this is not a serious limitation.)

As with the $N = 200$ simulations described above, initial structures were extracted from an equilibrated simulation of neat liquid water (SPC water model) with either $N = 300$ or 600 molecules in the unit cell. Trajectories were propagated for 80 ps, and as in the smaller unit cells the electron internalizes into the bulk in every single trajectory. Simulations were propagated for an additional 50 ps to equilibrate the internalized e^-(aq) for use in bulk

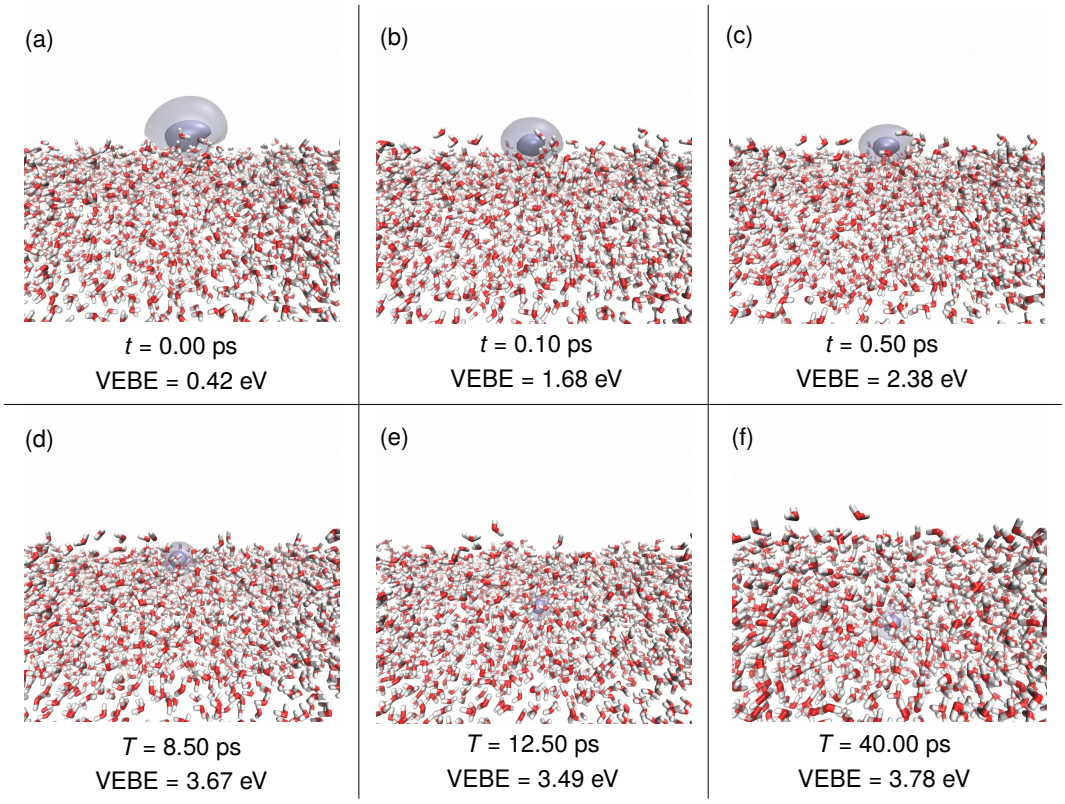

Figure S1: Snapshots from a simulation of an electron initialized delocalized in liquid water using the Turi-Borgis pseudopotential model. In each panel, the opaque blue isocontour of the wave function encapsulates 50% of the one-electron probability distribution $|\psi(\mathbf{r})|^2$, while the lighter translucent isosurface encloses 95%. At $t = 0$, the electron is initialized as a completely delocalized particle in liquid water, with $r_g \approx 6.78$ Å. After 100 fs the wave function has contracted to $r_g \approx 3.93$ Å, as seen in (b), while the VEBE has increased by 1.46 eV. By 500 fs, the wave function further contracts to $r_g \approx 3.12$ Å and resides ≈ 1.1 Å above the GDS. By $t = 8.50$ ps, the size of the wave function is comparable to the bulk species with $r_g = 2.45$ Å, and its centroid has moved to 1.50 Å below the GDS where water molecules surround the electron, such that the VEBE in (d) is 1.29 eV larger than that in (c), and is similar to the bulk value. Panel (e) shows a snapshot shortly before the electron internalizes, with its centroid situated 7.75 Å below the GDS and with a VEBE that is similar to the bulk value and essentially unchanged relative to that in (d). By $t = 40$ ps in (f), the electron centroid has been fluctuating around $d = -13.00$ Å for 28 ps with a VEBE that has fluctuated around the bulk value since $t \approx 8.50$ ps. An animation of this trajectory is available as a web enhanced object.

simulations, as discussed above, and the initial structures were randomly selected from the last 10 ps of these equilibration trajectories. The bulk simulations were also propagated for 80 ps.

It should be noted that the initialization procedure used in these simulations does not represent a simulation of electron injection into water, except possibly that of an electron with zero kinetic energy. Rather, we simulate adiabatic dynamics on the ground-state Born-Oppenheimer potential energy surface generated by the one-electron model Hamiltonian. At $t = 0$, the electron is found wherever the potential energy is low, and that is consistently found to be a surface trap state formed by dangling O–H moieties at the water/vacuum

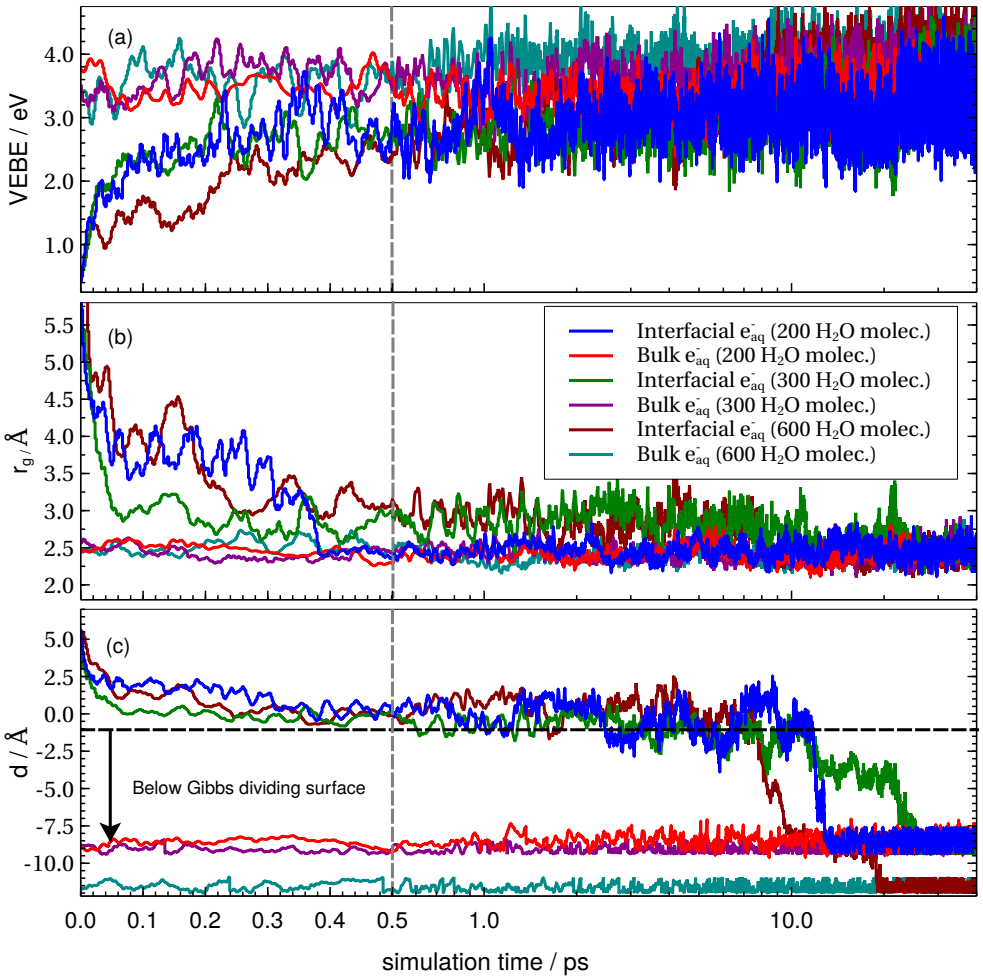

Figure S2: Time evolution of (a) the VEBE, (b) the radius of gyration (r_g), and (c) the distance (d) between the centroid of the e^-(aq) charge distribution and the Gibbs dividing surface from MD simulations employing a mean-field polarization potential model at ambient temperatures. (The time axis is linear for the first 0.5 ps then switches to a logarithmic scale.) For comparison to the simulations utilizing $N = 300$ and $N = 600$ water molecules, the data from representative $N = 200$ trajectories are reproduced from Fig. 2.

interface, as shown for example in Fig. 1(a). We have verified that different initial guesses for the wave function at $t = 0$ lead to the same solution, demonstrating that our eigensolver (the details of which are described in Ref. S3) is robust. For example, Fig. S1 is analogous to Fig. 1 but for a unit cell containing 600 water molecules, and with an initial guess wave function that is completely delocalized. Very similar localization and internalization dynamics can be seen in this trajectory as compared to that in Fig. 1.

Figure S2 shows representative trajectories for all three unit cell sizes, with the $N = 200$ trajectories being the same ones that are plotted in Fig. 2. Despite being initialized as a delocalized particle below the GDS, the interfacial e^-(aq) immediately appears as a diffuse charge cloud [$r_g \approx$ 5–6 Å, see Fig. S2(b)] located at $d \approx$ 3–6 Å above the liquid surface as illustrated in Fig. S1(a). This behavior is easily understood. Unlike in previous simulations of e^-(aq) in bulk water that used an isotropic unit cell (*i.e.*, no water/vacuum interface),

Table S1: Average values for selected observables from mean-field polarization model simulations with varying numbers of water molecules, N.

N	System	$\langle$VEBE$\rangle$ (eV)	$\langle r_g \rangle$ (Å)	$\langle d \rangle$ (Å)
200	interface[a]	3.13	2.55	−1.76
200	bulk	3.39	2.43	−8.46
300	interface[a]	3.34	2.49	−1.97
300	bulk	3.57	2.40	−8.78
600	interface[a]	3.67	2.44	−1.66
600	bulk	3.84	2.39	−13.01

[a] Averages exclude data points after the electron internalizes.

and for which the electron takes ∼1 ps to carve out and localize in an excluded volume,[S3] in the present simulations there exist, already at $t = 0$, shallow potential energy "traps" around dangling O–H moieties at the interface. The ground-state wave function at $t = 0$ occupies in these traps, one of which is apparently deep enough relative to the others such that the electron localizes in it, as shown in Fig. S1(a).

Essentially instantaneous electron localization is observed in every trajectory at every box size, as is the rapid increase in VEBE during the first 0.5 ps, as exemplified by panels (b) and (c) of Figs. 1 and S1. The internalization process is spontaneous on a timescale of 20–25 ps regardless of the size of the simulation cell or the initial conditions used to introduce the electron at $t = 0$, and upon internalization the electron fluctuates around $d \approx 9$–10 Å for $N = 200$ and $N = 300$ simulations and $d \approx 13$ Å for $N = 600$, which reflects half the thickness of the simulated water slab. (The $N = 200$ and $N = 300$ simulation cells are sufficiently similar in size, at $L_x = 18.1617$ and 20.7961 Å, respectively, that the 1.0–1.5 Å fluctuations about the midpoint blur the distinction and the electron fluctuates around similar values of d in both cases.) The good agreement that we see amongst all three simulation cell sizes is consistent with the fact that the potential of mean force for pulling an electron through the interface, which was computed in Refs. S18 and S19 using the same Turis-Borgis pseudopotential that is used here, flattens out at $d \approx 9.5$ Å, just slightly more than half the width of the slab in our smallest simulation cell.

Table S1 reports averages for the quantities r_g, VEBE, and d, comparing different simulation cell sizes from all twenty simulations. For each given box size, values of the VEBE and radius of gyration are rather similar, regardless of whether the electron was initialized in the bulk or at the interface, although the average VEBE for the interfacial species is about 0.2 eV smaller than that of the bulk species. As a test of convergence, we can throw out half of the trajectories and recompute the averages, and we find that they change hardly at all. Average VEBEs change by only about 0.05 eV and $\langle r_g \rangle$ by about 0.05 Å, for both the bulk and interfacial species. The average distance $\langle d \rangle$ to the GDS is essentially unchanged for the bulk species and changes by < 0.1 Å for the interfacial species. Full probability distributions for the bulk and interfacial VEBE are depicted in Fig. S3 and are fit quite well to Gaussian

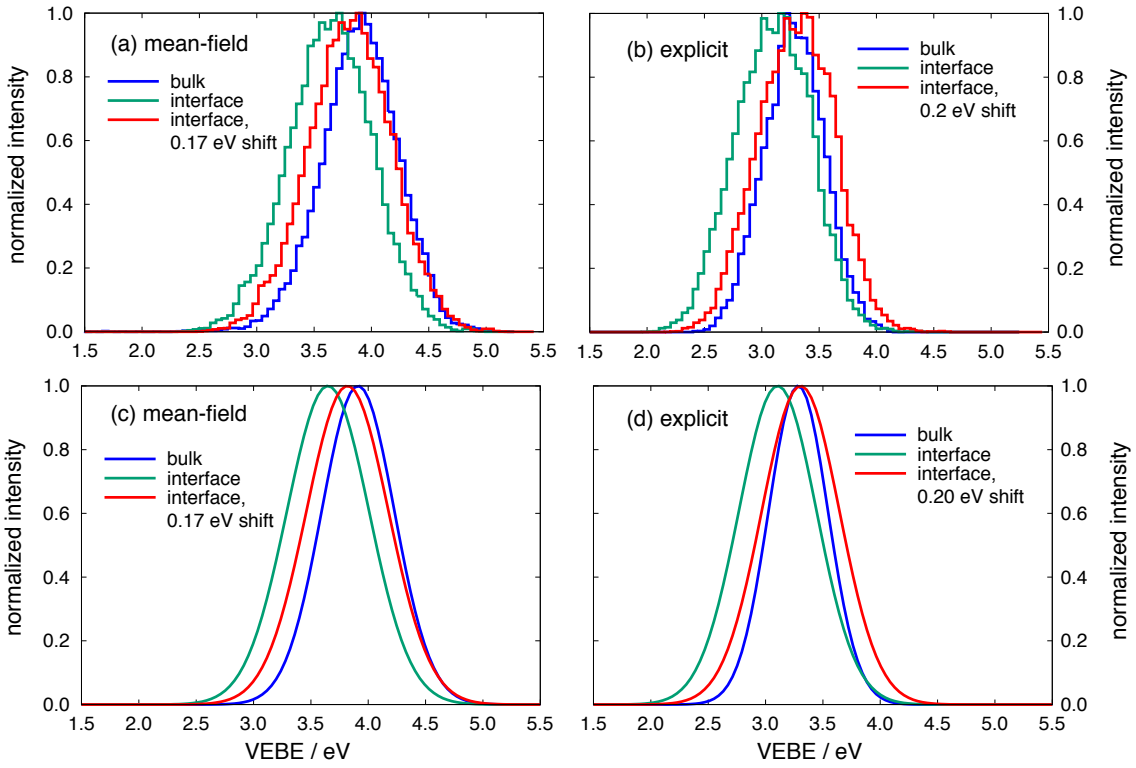

Figure S3: Probability distributions for the bulk and interfacial VEBE using (a) the mean-field polarization model, in an $N = 600$ water box; and (b) the explicit polarization model, in an $N = 200$ water box, with histogram bin widths of 0.05 eV in each case. Panels (c) and (d) show Gaussian fits to the data in (a) and (b), respectively. (Fitting parameters are listed in Table S2.) The interfacial distributions are also shown following a shift in energy equal to the difference in the mean VEBEs of the bulk and interfacial distributions, as reported in Tables 1 and S1. Differences in the center points of the distributions in (a) versus (b) are partly the result of the effects of finite box size.

probability distributions,

$$g(E) = \exp\left(\frac{-(E - \langle E\rangle)^2}{2\sigma^2}\right) , \tag{S1}$$

with fitting parameters given in Table S2. Although the distributions of interfacial VEBEs are 0.1–0.2 eV wider than those obtained in bulk water, we find that even in terms of the raw data both distributions look quite similar if the interfacial distribution is simply shifted 0.2 eV higher in energy, which is the difference in the mean VEBE at the interface relative to that in bulk water.

Table S2: Parameters for the Gaussian fits [Eq. (S1)] of the VEBE data in Fig. S3.

Polarization Method	System	Parameter (eV)		
		$\langle E\rangle$	σ	FWHM[b]
explicit	interface	3.1060	0.3392	0.7987
explicit	bulk[a]	3.2856	0.2596	0.6113
mean-field	interface	3.6489	0.3583	0.8437
mean-field	bulk[a]	3.9115	0.3175	0.7476

[a] Averages exclude data points after the electron internalizes.

[b] Full width at half maximum of the Gaussian distribution.

Very recently, Casey *et al.*,[S19] also reported distributions of bulk and interfacial VEBEs based on simulations employing the mean-field Turi-Borgis pseudopotential, but based on an alternative definition of the instantaneous liquid interface.[S40] (In our simulations, the Gibbs dividing surface is also updated at each time step.) The simulations and sampling protocol reported in Ref. S19 afford a shift approaching 0.5 eV between the interfacial and bulk VEBE distributions, as opposed to the 0.2 eV shift reported here. The reasons for this discrepancy are unclear, although there is certainly a tail in our interfacial VEBE distributions that is shifted much more than 0.5 eV from the mean value in bulk water, so it could simply be that the definition of the liquid surface that is used in Ref. S19 excludes more of the water molecules than does the Gibbs dividing surface, giving it a preference for identifying as "interfacial" simulation snapshots where the electron is more weakly solvated, as compared to those snapshots that the Gibbs surface identifies as interfacial. Tthe 0.2 eV shift that we obtain using both pseudopotential models agrees quantitatively with the shift obtained from DFT and MP2 calculations based on QM/MM trajectories; see Table 2.

The averages in Table S1 do show that the VEBE increases with box size, due to the importance of long-range Coulomb interactions in the ionization process, as we have reported previously.[S3] As in previous work,[S3] we can correct for this by extrapolating $\langle$VEBE$\rangle$ as a function of the inverse unit cell length, L_x^{-1}, and such an extrapolation is shown in Fig. S4. Remarkably, both the interfacial and bulk VEBE extrapolate essentially to the same value in the infinite-dilution limit: 4.87 eV for the interfacial species versus 4.85 eV for the bulk species. The extrapolated bulk value is also consistent with a previous extrapolation of 4.79 eV for the bulk species, using the same Turis-Borgis pseudopotential.[S3] When the VEBEs for large $(H_2O)_N^-$ clusters are extrapolated to $N \to \infty$ using the Turis-Borgis pseudopotential, a value of 4.4 eV is obtained for the interior (cavity) states, versus 3.9 eV for surface-bound electrons.[S41]

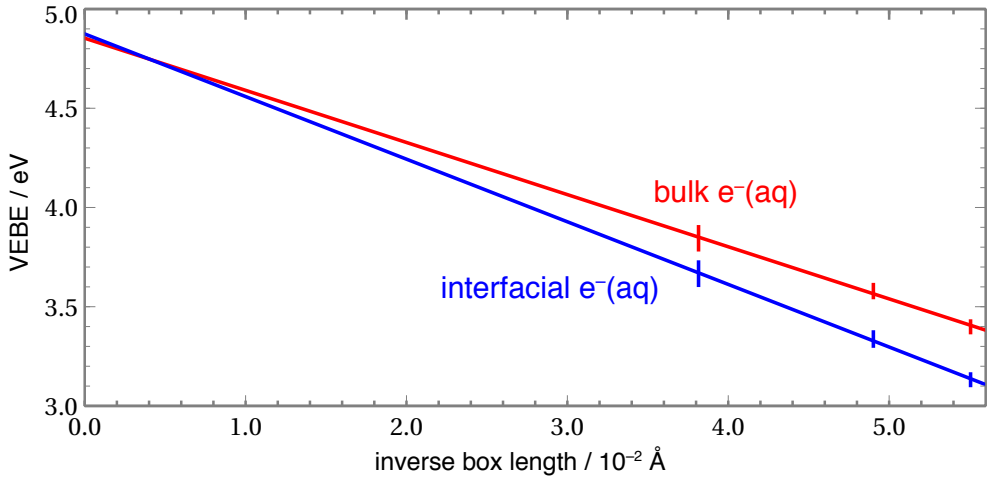

Figure S4: Extrapolation of the average VEBE computed using the mean-field polarization potential, as a function of the inverse unit cell length, L_x^{-1}. Error bars reflect a 95% confidence interval in $\langle \text{VEBE} \rangle$, which is averaged over trajectories and over time.

Each of these extrapolated values for the bulk VEBE is significantly larger than the accepted range of experimental values, 3.3–3.7 eV.[S42–S46] In Ref. S3, the infinite-dilution extrapolation was performed using the explicit polarization model (in addition to the mean-field Turi-Borgis model), and it was found that the electronic reorganization energy associated with relaxing the inducible dipole moments on the water molecules is significant, and reduces the VEBE by 1.37 eV in the limit $L \to \infty$. A very similar correction to the non-polarizable Turi-Borgis VEBE, 1.3 eV, was obtained using a continuum model,[S3] which inspires some confidence that this is indeed the electronic (clampled-nuclei) reorganization energy associated with vertical ionization of $e^-(aq)$. A correction of 1.3 eV applied to the extrapolated Turis-Borgis VEBE from Fig. S4 affords a corrected VEBE of 3.6 eV, within the experimental range.

2 DFT and MP2 Calculations

2.1 Density Functionals

DFT calculations reported in this work use a long-range-corrected (LRC) version of the "BOP" density functional. The BOP functional is comprised of Becke's generalized-gradient exchange functional (B88),[S22] along with the "one-parameter progressive" (OP) correlation functional,[S23] which is similar to the more familiar Lee-Yang-Parr (LYP) correlation functional.[S24] The resulting exchange-correlation functional is

$$E_{xc}^{\text{LRC-}\mu\text{BOP}} = E_c^{\text{OP}} + E_x^{\mu\text{B88,SR}} + E_x^{\text{HF,LR}}, \tag{S2}$$

where "SR" and "LR" express that only the short-range or long-range parts of the Coulomb operator are employed when evaluating these components of the energy. The functional in Eq. (S2) has been implemented[S25,S26] in the Q-Chem electronic structure program,[S27]

where it is called LRC-μBOP.[S28] This functional has been shown to afford accurate VEBEs for $(H_2O)_N^-$ clusters as compared to correlated wave function benchmarks.[S5,S29]

The range-separation parameter, μ, dictates the partition between what is considered short-range versus long-range in the Coulomb operator. (Roughly speaking, this partition occurs on a length scale $\sim \mu^{-1}$.) Baer and co-workers[S30] suggest a non-empirical "tuning" procedure to determine μ, according to the criterion

$$\mathrm{IE}_{\Delta\mathrm{SCF}}(\mu) = -\epsilon_{\mathrm{SOMO}}(\mu) \; . \tag{S3}$$

Here, ϵ_{SOMO} represents the self-consistent field (SCF) orbital energy for the singly-occupied molecular orbital (SOMO) and $\mathrm{IE}_{\Delta\mathrm{SCF}}$ is the ionization energy determined from a "ΔSCF" approach, *i.e.*,

$$\mathrm{IE}_{\Delta\mathrm{SCF}}(\mu) = E_{\mathrm{neutral}}(\mu) - E_{\mathrm{anion}}(\mu) \; . \tag{S4}$$

(The neutral and anion energies are computed at the geometry of the anion.) The condition in Eq. (S3) is a rigorous one for the exact Kohn-Sham functional, and because the ionization energy (IE) controls the long-range decay of the SCF wave function, this tuning procedure ensures an exchange-correlation potential with proper long-range behavior.[S31]

Unfortunately, the optimally-tuned value of μ is known to exhibit a strong dependence on system size,[S28,S32–S34] even for chemically homologous systems. In previous QM/MM calculations of the bulk and interfacial hydrated electron, we have shown that μ should be tuned separately for each distinct size of the QM region.[S33] This leads to an electronic absorption spectrum for e^-(aq) in bulk water that is in excellent agreement with the experimental spectrum, whereas values of μ that are tuned for small clusters afford a significantly shifted spectrum, as do global hybrid functionals such as B3LYP.[S17,S33]

We use QM regions that range in size from a radius of 5.5–8.0 Å around the centroid of the spin density, and we tune μ separately for each different size. Figure S5 demonstrates the tuning procedure for three snapshots containing 47–50 QM water molecules, corresponding to a QM radius of 7.5 Å, extracted from an *ab initio* simulation of interfacial e^-(aq).[S36] Each of the three snapshots is separated in time by 4 ps. As μ increases (and thus Hartree-Fock exchange is introduced on increasingly short length scales), the SOMO is increasingly destabilized. This is the result of eliminating self-interaction error associated with the unpaired electron, which is primarily a long-range phenomena for this particular system since the unpaired electron exists largely outside of the valence-electron regions of the water molecules. The IE, in contrast, is less sensitive to changes in μ. In order to satisfy the criterion of Eq. (S3) in an average way across all three snapshots in Fig. S5, we set $\mu = 0.18\ a_0^{-1}$. The value of μ used for each QM size for both the bulk and interfacial species was determined independently using this procedure. These "tuned" values of μ are listed in Table S3.

In a recent study of the optical spectrum of e^-(aq) using time-dependent DFT (TD-DFT),[S33] we showed that this spectrum is sensitive to the value of μ, and that the spectrum is significantly blue-shifted (as compared to experiment) for $\mu \gtrsim 0.3\ a_0^{-1}$. This is despite the fact that values of $\mu > 0.3\ a_0^{-1}$ afford accurate VEBEs for small, gas-phase $(H_2O)_N^-$ clusters.[S5,S29] These discrepancies in the optical spectrum (with respect to experiment) are not reconciled by increasing the size of the QM region.[S33] In Ref. S33, a range-separation parameter $\mu = 0.165\ a_0^{-1}$ was ultimately chosen based on the tuning procedure described

System	QM region radius/Å	$\langle N \rangle$	μ/ a_0^{-1}	VEBE / eV		PCM Correction / eV		Poisson Correction/ eV	
				DFT	MP2	DFT	MP2	DFT	MP2
interface	5.5	21	0.205	2.05 ± 0.38	1.96 ± 0.37	–	–	1.05	1.11
interface	6.0	26	0.195	2.17 ± 0.39	2.05 ± 0.38	–	–	1.01	0.97
interface	6.5	32	0.190	2.22 ± 0.37	2.11 ± 0.34	–	–	0.94	0.95
interface	7.0	39	0.185	2.30 ± 0.33	2.20 ± 0.33	–	–	0.87	0.88
interface	7.5	47	0.180	2.37 ± 0.34	2.26 ± 0.35	–	–	0.77	0.83
interface	8.0	58	0.170	2.45 ± 0.33	2.35 ± 0.33	–	–	0.74	0.75
bulk	5.5	29	0.195	2.12 ± 0.29	2.04 ± 0.31	1.40	1.40	1.21	1.14
bulk	6.0	37	0.180	2.31 ± 0.32	2.22 ± 0.34	1.30	1.20	1.05	0.99
bulk	6.5	47	0.175	2.36 ± 0.31	2.29 ± 0.37	1.21	1.08	1.01	0.88
bulk	7.0	58	0.170	2.40 ± 0.32	2.33 ± 0.33	1.13	1.08	0.97	0.86
bulk	7.5	71	0.165	2.49 ± 0.35	2.39 ± 0.32	1.10	1.03	0.86	0.81
bulk	8.0	86	0.160	2.58 ± 0.33	2.51 ± 0.31	0.95	0.94	0.80	0.71

Table S3: Average number of water molecules, $\langle N \rangle$, and optimally-tuned range-separation parameters, μ, for LRC-μBOP. Also shown are the average VEBEs for these QM regions, computed at the LRC-μBOP/ and RI-MP2/6-31++G* levels of theory. (Uncertainties represent one standard deviation, averaged over snapshots extracted from the simulations.) In these calculations, the QM region is treated as a gas-phase $(H_2O)_N^-$ cluster, *i.e.*, the QM regions are the same as in the calculations presented in Table 2 but the latter calculations include PCM boundary conditions. Comparison of these "gas phase" values with the results in Table 2 affords the PCM corrections that are listed here, which illustrate the magnitude of the correction for long-range electrostatic effects.

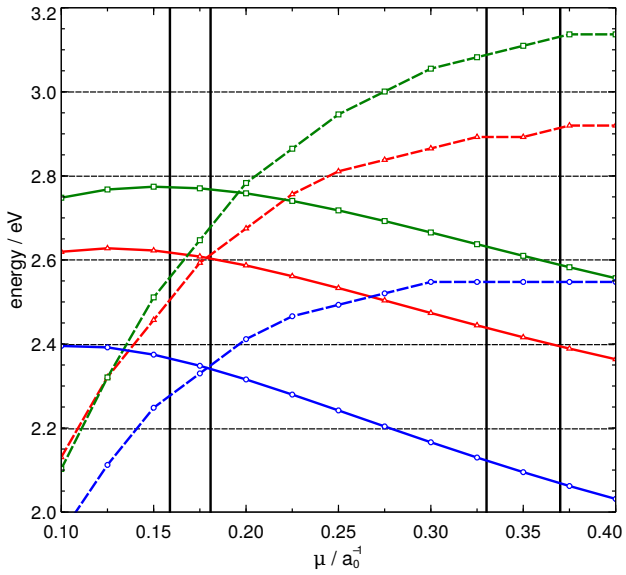

Figure S5: Illustration of the tuning procedure for LRC-μBOP/6-31++G*, demonstrated for three different $(H_2O)_N^-$ geometries (with $N = 47$–50) that are shown in red, blue, and green and were extracted from an *ab initio* interfacial e^-(aq) simulation.[S36] The solid curves represent $IE_{\Delta SCF}(\mu)$ and the dashed curves are $-\epsilon_{SOMO}(\mu)$. Where the dashed and solid curves of a particular color intersect is the "optimally tuned" value of μ for that particular snapshot, and in this case we choose $\mu = 0.18$ a_0^{-1} as the best compromise value for these three snapshots. This value is indicated by a vertical line, and the other vertical lines indicate other values of μ that have been employed in previous hydrated-electron studies using this functional. These include $\mu = 0.165$ a_0^{-1} (Ref. S33), $\mu = 0.33$ a_0^{-1} (Ref. S29), and $\mu = 0.37$ a_0^{-1} (Refs. S13 and S16).

above (see Table S3). We emphasize that this tuning procedure needs to be performed separately at each unique QM system size, and we have done so here. Evident from Table S3 is a small but clear anti-correlation between the number of QM water molecules and the optimally-tuned value of μ.

In addition to listing the optimally-tuned values of μ, Table S3 provides the average VEBE computed for the gas-phase QM region, *i.e.*, a negatively-charged water cluster with vacuum boundary conditions. As in Table 2, these calculations are performed at both the LRC-μBOP/6-31++G* level of theory and the resolution-of-identity (RI)-MP2/6-31++G* level. For each snapshot (extracted from the QM/MM simulations reported in Refs. S35 and S36), the Turi-Borgis pseudopotential model[S1] was employed to estimate the centroid of the spin density, and then all water molecules contained within a sphere centered at this point were included in the QM region for the DFT or MP2 calculations. We vary the radius of this sphere to watch the convergence of the VEBE with respect to the size of the QM region. The average number of H_2O molecules contained in this sphere is shown as $\langle N \rangle$ in Table S3.

Note that the only difference between the calculations reported in Table S3 and those in Table 2 is that in the latter case, continuum boundary conditions are applied in order to obtain quantitative agreement with experiment, whereas in Table S3 the QM region is treated as a gas-phase $(H_2O)_N^-$ cluster. Comparison of the two data sets allows us to assess the quantitative importance of the boundary conditions. We find that the non-equilibrium solvation model increases the VEBE by ≈ 0.7–1.1 eV for the interfacial species and by ≈ 0.7–1.4 eV for e^-(aq) in bulk water. Notably, the VEBE converges more rapidly, as a function of

Table S4: Average VEBEs computed using two different basis sets, for the interfacial hydrated electron (computed using the DFT/Poisson method) and the bulk hydrated electron (computed using the DFT/PCM method).

System	QM radius/ Å	VEBE / eV	
		6-31++G*	6-31(1+,3+)G*
interface	5.5	3.15 ± 0.41	3.18 ± 0.43
interface	7.5	3.14 ± 0.41	3.16 ± 0.44
bulk	5.5	3.52 ± 0.31	3.55 ± 0.33
bulk	7.5	3.59 ± 0.35	3.62 ± 0.30

the size of the QM region, for calculations that use continuum boundary conditions (Table 2) than it does for calculations with vacuum boundary conditions (Table S3), suggesting that the dielectric continuum is providing the desired long-range electrostatic effect of the bulk solvent.

2.2 Basis Sets

We used the 6-31++G* basis set to compute VEBEs in Tables 2 and S3, as in previous simulations of the optical spectrum of e^-(aq).[S13,S17,S33] The choice of basis set has been carefully examined in previous work[S17,S31,S33,S37–S39] (see Ref. S17 in particular), with the conclusion that in a condensed-phase aqueous environment, convergence of the VEBE is rapid and requires only a single set of diffuse basis functions, despite the fact that the electron occupies an excluded volume in the structure of liquid water. Additional diffuse shells have a very limited effect.[S17]

Nevertheless, to test basis-set effects in the present context we computed VEBEs using the 6-31(1+,3+)G* basis set,[S38] which includes two additional diffuse shells as compared to 6-31++G*, with exponents of $\zeta_1 = 0.2700058\ a_0^{-2}$ and $\zeta_2 = 0.0845\ a_0^{-2}$ that are reduced by successive factors of 3.2 relative to the most diffuse exponent in the 6-31++G* basis set. Results are listed in Table S4. Only minor deviations of ≈ 0.03 eV are observed between the two basis sets, and we thus regard the 6-31++G* basis set as being sufficiently diffuse.

3 Non-Equilibrium Continuum Solvation Models

The DFT and MP2 calculations described above were performed on snapshots extracted from the QM/MM simulations reported in Refs. S35 and S36. Although we use large QM regions in these single-point calculations—up to a radius of 8.0 Å, which encompasses ≈ 90 QM water molecules—longer-range polarization effects must still be incorporated in order to obtain a VEBE that is in quantitative agreement with the consensus value for e^-(aq) in bulk water. This is evident in the fact that the VEBE changes by $\sim$1 eV between the $N = 600$ simulation cell and the infinite-dilution limit; see Fig. S4. (The difference is smaller, but still not negligible, when a polarizable pseudopotential model is employed.[S3]) This speaks to the importance of very long-range Coulomb effects on the VEBE.

The dielectric continuum models described below are a less-expensive substitute for this type of extrapolation, designed for use with an all-electron QM treatment of some number of explicit water molecules. Two such models are described here: the "polarizable continuum model" (PCM)[S47,S48] that is familiar in quantum chemistry calculations and which is designed to approximate isotropic (bulk) solvation effects, and also direct numerical solution of Poisson's equation.[S49] The latter method can be used in non-homogeneous dielectric environments such as the water/vacuum interface. In each case, we use a "non-equilibrium" version of the continuum solvation model,[S50,S51] as appropriate for description of a vertical (rather than an adiabatic) ionization process.

3.1 PCM for Isotropic Solvation

The specific version of PCM employed here for the bulk species e^-(aq) is the "integral equation formalism", IEF-PCM.[S48,S52–S54] The *equilibrium* version of IEF-PCM affords aqueous solvation free energies within a few kcal/mol of experimental values for small to medium-size molecules and ions, if non-electrostatic corrections are applied,[S55–S57] but accurate solvatochromatic shifts can be obtained without such corrections, using the non-equilibrium version of the model.[S50] The non-equilibrium model is designed to describe electronic polarization of the solvent upon vertical excitation or ionization of the solute.[S58–S61] In other words, while the ionization process may be vertical (in the sense that the vibrational and orientational degrees of freedom of the solvent molecules are not allowed to relax or respond in any way), electronic polarization of the solvent should take place on the same time scale as excitation or ionization and ought to be considered, even in a continuum treatment. This effect is represented by re-polarizing the continuum solvent in the excited state of the solute using the solvent's *optical* (rather than static) dielectric constant, $\epsilon_\infty = n^2$, where n is the solvent's index of refraction. The total polarization response of the solvent is partitioned into a "fast" component (due to the electrons and described using $\epsilon_\infty = 1.8$ for water) and a "slow" component (due to nuclear reorganization and described using $\epsilon_{\text{static}} = 78.39$ for water). Details of the non-equilibrium PCM and its implementation in Q-Chem[S27] can be found in Refs. S50 and S51.

The predictions of PCM-type methods are sensitive to the details of how the "solute cavity" (*i.e.*, the boundary between the atomistic QM region and the continuum solvent) is constructed. Most often this cavity is taken to be a union of atom-centered spheres, whose radii may be considered to be parameters of the model. The calculations presented here, however, include a large number of explicit water molecules, obviating the need for such crude boundary conditions. These are suspect anyway for a species like e^-(aq) where one electron is clearly outside of the van der Waals radii of the atoms and would therefore directly inhabit in continuum region. Moreover, in the presence of explicit solvent molecules, the aforementioned "van der Waals" cavity construction places dielectric medium between the explicit solvent molecules, which should not be there since Coulomb interactions are treated explicitly in the QM region.

As an alternative, we use a QM/continuum interface consisting of single sphere whose radius is selected to be 2.75 Å larger than the radius of the QM region. (The QM radii are reported in Table 2.) This cavity is discretized using a Lebedev integration grid with 5,294 points. The 2.75 Å buffer reflects the estimated diameter of a water molecule, according

to effective ionic radii for the isoelectronic ions O^{2-}, OH^-, and H_3O^+.[S62] In addition, our selection criterion for placing H_2O molecules in the QM region is to do so if any one of the three atoms lies within the specified QM radius, and as such there are cases where a hydrogen nucleus ends up as much as 2.75 Å farther away from the origin than the proscribed radius of the QM region. In any case, the predicted VEBEs are relatively insensitive to small changes in the size of the spherical cavity provided that it encompasses the entire QM region. (When QM nuclei extend beyond the cavity, non-sensical results are obtained or in some cases the SCF + PCM procedure fails to converge at all.)

3.2 Poisson's Equation for Anisotropic Solvation

PCMs are appropriate for describing e^-(aq) in isotropic bulk solution, but not at the anisotropic water/vacuum interface. At the interface, we resort to solving Poisson's equation,

$$\hat{\boldsymbol{\nabla}} \cdot \Big[\epsilon(\mathbf{r})\hat{\boldsymbol{\nabla}}\varphi(\mathbf{r})\Big] = -4\pi\rho(\mathbf{r}) \;, \tag{S5}$$

for the electrostatic potential $\varphi(\mathbf{r})$. The quantity $\rho(\mathbf{r})$ in this equation is the QM charge density, including both nuclei and electrons. This density is embedded in a dielectric medium described by a spatially-inhomogeneous dielectric function, $\epsilon(\mathbf{r})$. Given a spatially *homogeneous* dielectric function, solution of Eq. (S5) should afford a solvation energy

$$G = \tfrac{1}{2}\int d\mathbf{r}\; \varphi(\mathbf{r})\; \rho(\mathbf{r}) \tag{S6}$$

that is equivalent to the PCM solvation energy, up to discretization errors that can be made quite small,[S48,S54] and neglecting "volume polarization" arising from the tails of the QM wave function that penetrate beyond the solute cavity.[S48,S63,S64] Volume polarization effects can be significant for anions but are mitigated here by the use of a large number of QM water molecules, such that the diffuse e^-(aq) wave function has likely decayed to zero well before reaching the QM/continuum interface. This expectation is confirmed by the rapid convergence of the VEBE with respect to the size of the QM region that is reported in Table 2.

For this work, we have developed a QM/Poisson approach to non-equilibrium solvation, based on the non-equilibrium polarization formalism described in Refs. S50 and S51. The difference in the present work is that whereas Refs. S50 and S51 (along with other works on non-equilibrium solvation[S58–S61]) are couched in terms of a so-called *apparent surface charge* PCM,[S47,S48] in which only the two-dimensional solute/continuum interface (solute cavity surface) must be discretized, here we describe the polarization response to vertical detachment of the electron in terms of three-dimensional charge densities. This modification is necessary in order to describe the anisotropic case. The resulting QM/Poisson approach has been implemented in a locally-modified version of the Q-Chem electronic structure program,[S27] following the algorithm in Ref. S49, and is described in more detail below.

3.2.1 Discretization of the Density

To solve Eq. (S5), we discretize the QM electron density $\rho_{\text{elec}}(\mathbf{r})$ on a 25 Å × 25 Å × 25 Å Cartesian grid with a grid spacing of $\Delta x = 0.22$ Å in each direction, which closely follows the details of both the classical electrostatics calculations reported in Ref. S65 (although the grid used here is slightly more conservative, reflecting the somewhat more complicated topology of the electrostatic potential generated by a QM charge distribution[S66]) as well as those of the quantum electrostatics calculations reported in Refs. S49 and S67. The Turi-Borgis pseudopotential model[S1] is used to estimate the location of the centroid of the spin density, for reasons of computational expediency, and this point is selected as the origin for the grid.

Following Ref. S49, the total density on the grid is separated into two parts: ρ_{solute}, which consists of the electronic and nuclear charge contributions from the solute (QM region), and ρ_{pol}, a polarization charge density arising from interactions with the dielectric medium. In detail,

$$\begin{aligned} \rho_{\text{tot}}(\mathbf{r}) &= \rho_{\text{elec}}(\mathbf{r}) + \rho_{\text{nuc}}(\mathbf{r}) + \rho_{\text{pol}}(\mathbf{r}) \\ &= \rho_{\text{solute}}(\mathbf{r}) + \rho_{\text{pol}}(\mathbf{r}) \end{aligned} \tag{S7}$$

where

$$\rho_{\text{solute}}(\mathbf{r}) = \rho_{\text{elec}}(\mathbf{r}) + \rho_{\text{nuc}}(\mathbf{r}) \tag{S8}$$

is the charge density of the QM region. Its electronic part is

$$\rho_{\text{elec}}(\mathbf{r}) = -\sum_{\mu\nu}^{N_{\text{basis}}} P_{\mu\nu}\, g_\mu(\mathbf{r})\, g_\nu(\mathbf{r}) \;, \tag{S9}$$

where $\mathbf{P}$ is the one-electron density matrix and g_μ is an atom-centered Gaussian basis function.

The point charge Z on a given nucleus can lead to singularities in grid-based solutions of Poisson's equation. Following the procedure used in Ref. S65 for classical atom-centered point charges, we therefore add the nuclear charge Z to the nearest Cartesian grid point but with a value $Z/(\Delta x)^3$ that reflects the smearing of this charge over one voxel of the Cartesian grid. Formally, this means that we represent the nuclear contribution to the charge density as

$$\rho_{\text{nuc}}(\mathbf{r}) = \sum_{A}^{\text{atoms}} \left(\frac{Z_A}{(\Delta x)^3} \right) \delta\left(\mathbf{r} - \mathbf{R}_A\right) \;, \tag{S10}$$

where $\mathbf{R}_A$ is the position vector of the Cartesian grid point nearest to nucleus A.

3.2.2 Numerical Solution of Poisson's Equation

We first solve the Poisson equation

$$\hat{\nabla}^2 \varphi_{\text{solute}}(\mathbf{r}) = -4\pi \rho_{\text{solute}}(\mathbf{r}) \tag{S11}$$

for the solute's electrostatic potential in vacuum, $\varphi_{\text{solute}}(\mathbf{r})$. This is accomplished using a finite-difference, pre-conditioned conjugate gradient algorithm adapted from Ref. S49. Convergence is achieved when the residual vector reaches a Euclidean norm of 10^{-5} a.u. Having determined the electrostatic potential of the solute in vacuum, Poisson's equation

$$\begin{aligned}\hat{\boldsymbol{\nabla}} \cdot \Big[\epsilon(\mathbf{r})\hat{\boldsymbol{\nabla}}\varphi_{\text{tot}}(\mathbf{r})\Big] &= -4\pi\rho_{\text{tot}}(\mathbf{r}) \\ &= -4\pi\Big[\rho_{\text{solute}}(\mathbf{r}) + \rho_{\text{pol}}(\mathbf{r})\Big]\end{aligned} \tag{S12}$$

is then solved in the presence of a spatially-inhomogeneous dielectric function $\epsilon(\mathbf{r})$, in order to obtain the polarization charge density and the corresponding polarization potential. We separate the polarization charge density into two contributions, as follows:

$$\rho_{\text{pol}}(\mathbf{r}) = \rho_{\text{iter}}(\mathbf{r}) + \left(\frac{1-\epsilon(\mathbf{r})}{\epsilon(\mathbf{r})}\right)\rho_{\text{solute}}(\mathbf{r}) \; . \tag{S13}$$

The iterative charge density $\rho_{\text{iter}}(\mathbf{r})$ is induced by the dielectric function acting over the whole simulation grid, and acts as an additional source term to the total charge density for Poisson's equation.[S49,S67] The second term in Eq. (S13) is a scaled solute charge density.

To iterate $\rho_{\text{iter}}(\mathbf{r})$ to convergence, we perform updates $\rho_{\text{iter}}^{(i)} \rightarrow \rho_{\text{iter}}^{(i+1)}$ where

$$\rho_{\text{iter}}^{(i+1)}(\mathbf{r}) = \frac{1}{4\pi}\Big[\hat{\boldsymbol{\nabla}}\ln\epsilon(\mathbf{r})\Big] \cdot \Big[\hat{\boldsymbol{\nabla}}\varphi_{\text{tot}}^{(i)}(\mathbf{r})\Big] \; . \tag{S14}$$

[Note that $\rho_{\text{pol}}(\mathbf{r}) = \rho_{\text{iter}}(\mathbf{r})$ at any point $\mathbf{r}$ for which $\epsilon(\mathbf{r}) = 1$.] Once the solute's electrostatic potential is obtained in vacuum, the polarization charge density is updated according to Eq. (S13) and then the total charge density is constructed using Eq. (S7). The latter is the density utilized in solving Poisson's equation, Eq. (S5).

For the first iteration of the conjugate gradient routine ($i = 0$), the total electrostatic potential in Eq. (S14) is simply the solute's "gas-phase" (vacuum boundary conditions) electrostatic potential. Subsequently, Eq. (S12) is solved for the total electrostatic potential using the total charge density at the current iteration, and this in turn is used to update the iterative charge density via Eq. (S14). Following the procedure outlined in Refs. S49 and S67, a damping procedure is applied to stabilize the updates $\rho_{\text{iter}}(\mathbf{r})$ in Eq. (S14). This consists of a linear combination of the densities at iterations i and $i+1$:

$$\begin{aligned}\rho_{\text{iter}}^{(i+1)}(\mathbf{r}) &= \frac{\eta}{4\pi}\Big[\hat{\boldsymbol{\nabla}}\ln\epsilon(\mathbf{r})\Big] \cdot \Big[\hat{\boldsymbol{\nabla}}\varphi_{\text{tot}}^{(i)}(\mathbf{r})\Big] + (1-\eta)\,\rho_{\text{iter}}^{(i)}(\mathbf{r}) \\ &= \eta\rho_{\text{iter}}^{(i+1)} + (1-\eta)\,\rho_{\text{iter}}^{(i)}(\mathbf{r}) \; .\end{aligned} \tag{S15}$$

We take $\eta = 0.6$. The iterative charge density, and therefore the polarization charge density, is updated until the Euclidean norm of the residual vector between iterations falls below a threshold of 10^{-5} a.u.

Once the total electrostatic potential and polarization response arising from the dielectric medium are known, the solute electrostatic energy can be computed:

$$E_{\text{elst}} = \tfrac{1}{2}\int d\mathbf{r}\; \varphi_{\text{tot}}(\mathbf{r})\; \rho_{\text{solute}}(\mathbf{r}) \; . \tag{S16}$$

Exploiting the density partition in Eq. (S7) along with the linearity of Poisson's equation, we can express the total electrostatic potential as $\varphi_{\rm tot}(\mathbf{r}) = \varphi_{\rm solute}(\mathbf{r}) + \varphi_{\rm pol}(\mathbf{r})$, which affords

$$\begin{aligned} E_{\rm elst} &= \tfrac{1}{2}\int d\mathbf{r}\; \varphi_{\rm solute}(\mathbf{r})\; \rho_{\rm solute}(\mathbf{r}) + \tfrac{1}{2}\int d\mathbf{r}\; \varphi_{\rm pol}(\mathbf{r})\; \rho_{\rm solute}(\mathbf{r}) \\ &= E_{\rm solute} + G_{\rm pol}\;. \end{aligned} \tag{S17}$$

The first term, $E_{\rm solute}$, represents the solute charge density interacting with its own electrostatic potential. This is equivalent to the explicit inter-particle Coulomb interactions that are already handled by the QM description of the solute. The second term,

$$G_{\rm pol} = \tfrac{1}{2}\int d\mathbf{r}\; \varphi_{\rm pol}(\mathbf{r})\; \rho_{\rm solute}(\mathbf{r}) \tag{S18}$$

represents the additional electrostatic stabilization engendered by the QM solute charge density interaction with the polarization response of the dielectric medium.

Note that $\varphi_{\rm tot}(\mathbf{r})$ and $\rho_{\rm tot}(\mathbf{r})$ are computed self-consistently at each SCF iteration. To properly incorporate solvent polarization effects, $\varphi_{\rm pol}(\mathbf{r})$ must be added to the effective Kohn-Sham Hamiltonian, which constitutes a solvation correction to the Fock matrix. This correction is equal to the functional derivative $\delta G_{\rm pol}/\delta\rho$, or in matrix form it is a correction $\mathbf{\Delta F}$ having matrix elements

$$\Delta F_{\mu\nu} = \int d\mathbf{r}\; \varphi_{\rm pol}(\mathbf{r})\; g_\mu(\mathbf{r})\; g_\nu(\mathbf{r})\;. \tag{S19}$$

The quantity $G_{\rm pol}$ should be added to the SCF energy. An outline of the QM/Poisson SCF algorithm appears as Algorithm 1 on pg. S19.

3.2.3 Dielectric Function

In order to describe anisotropic dielectric environments, we employ a dielectric function $\epsilon(\mathbf{r})$ that can assume a different value at each grid point in three-dimensional space. For testing and comparison purposes we have also implemented this approach for *isotropic* solvation, which we describe first. For e^-(aq) in bulk water, we imagine a spherical cavity whose radius is 2.75 Å larger than the radius of the QM region ($r_{\rm QM}$), as in the PCM calculations described in Section 3.1. Across this boundary, we interpolate $\epsilon(\mathbf{r})$ between the values $\epsilon_{\rm vac} = 1.0$ inside the cavity, where matter is described atomistically, and $\epsilon_{\rm static} = 78.39$ outside the cavity. (This smooth change in the dielectric aids with convergence of the finite-difference Poisson solver.[S68,S69]) Interpolation is accomplished as a function of the radial distance r from the center of the grid using a hyperbolic tangent switching function. In detail, the r-dependent dielectric function that we use is

$$\epsilon(r) = \frac{1}{2}\Big\{\epsilon_{\rm static} + \epsilon_{\rm vac} + (\epsilon_{\rm static} - \epsilon_{\rm vac})\tanh\Big[\alpha(r - r_{\rm mid})\Big]\Big\}\;. \tag{S20}$$

The parameter $\alpha = 3.9$ Å^{-1} controls the length scale of the switching process and $r_{\rm mid}$ is the midpoint of the interpolation. We take $r_{\rm mid} = r_{\rm QM} + 1.375$ Å, so that the dielectric assumes the value $\epsilon = (\epsilon_{\rm vac} + \epsilon_{\rm static})/2$ halfway between $r_{\rm QM}$ and $r_{\rm cavity} = r_{\rm QM} + 2.75$ Å. (See Fig. S6 for an example.) Numerical results are not strongly dependent on the details of

Algorithm 1: Equilibrium QM/Poisson SCF Procedure

Data: If feasible, precompute the value of $g_\mu(\mathbf{r}_i)$ at each grid point $\mathbf{r}_i$ for each basis function g_μ.

`/* This requires` $N_{\text{grid}} \times N_{\text{basis}}$ `storage, and if this is not feasible then the basis function values can instead be computed on-the-fly at each SCF iteration. */`

begin SCF procedure
  Initialize $\Delta\mathbf{F} \equiv 0$.
  repeat $n = 1, 2, \ldots$ SCF iterations
    Diagonalize the Fock matrix $\mathbf{F} = \mathbf{F}_0 + \Delta\mathbf{F}$ to obtain the density matrix $\mathbf{P}^{(n)}$, where $\mathbf{F}_0$ is the gas-phase Fock matrix and $\Delta\mathbf{F}$ is the solvation correction.
    Compute the electronic and nuclear charge densities at each grid point using Eqs. (S9) and (S10), and the solute charge density using Eq. (S8).
    begin Finite-difference Poisson solver
      Use the conjugate gradient Poisson solver (adapted from Ref. S65) to compute $\varphi_{\text{solute}}(\mathbf{r})$ with $\epsilon(\mathbf{r}) \equiv 1$.
    Use $\varphi_{\text{solute}}(\mathbf{r})$ to form $\rho_{\text{iter}}(\mathbf{r})$ and update $\rho_{\text{tot}}(\mathbf{r})$.
    repeat $i = 1, 2, \ldots$ Poisson solver iterations
      begin Electrostatic potential solver
        Compute $\varphi^{(i)}_{\text{tot}}(\mathbf{r})$ using Eq. (S12) and dielectric function $\epsilon(\mathbf{r})$.
        `// The form of the dielectric function is discussed in Section 3.2.3.`
      Use $\varphi^{(i)}_{\text{iter}}$ to form the updated density $\rho^{(i+1)}_{\text{iter}}$ [Eq. (S15)]. Also update ρ_{pol} [Eq. (S13)] and ρ_{tot} [Eq. (S7)].
    until $||\rho^{(i+1)}_{\text{iter}}(\mathbf{r}) - \rho^{(i)}_{\text{iter}}(\mathbf{r})|| < 10^{-5}$ a.u.
    Compute $\varphi_{\text{pol}} = \varphi_{\text{tot}} - \varphi_{\text{solute}}$.
    Generate the Fock matrix correction in Eq. (S19).
    Compute the polarization free energy G_{pol} [Eq. (S18)] and add it to the SCF energy.
  until *DIIS error* $< 10^{-5}$ a.u.

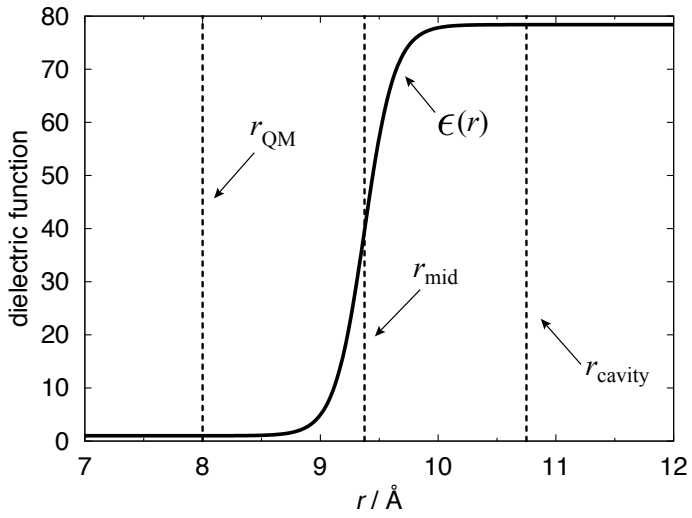

Figure S6: Dielectric function $\epsilon(r)$ from Eq. (S20), as a function of the distance r from the center of the QM region. The parameters of the switching function are $\alpha = 3.9$ Å^{-1} and $r_{\mathrm{mid}} = 9.375$ Å, as used in this work for a QM radius of 8.0 Å. In this example, $\epsilon(r_{\mathrm{QM}}) = 1.002$, $\epsilon(r_{\mathrm{mid}}) = 39.695$, and $\epsilon(r_{\mathrm{cavity}}) = 78.388$.

this smoothing procedure, and the calculations reported in Table 2 for e^-(aq) in bulk water demonstrate the extent to which IEF-PCM results agree with this QM/Poisson procedure.

The QM/Poisson procedure for the interfacial species is similar. We first use the Turi-Borgis model to estimate the center point of the electronic wave function and thus locate the center of the grid. Across a spherical cavity of radius $r_{\mathrm{cavity}} = r_{\mathrm{QM}} + 2.75$ Å surrounding the Turi-Borgis centroid, we smoothly interpolate $\epsilon(r)$ as indicated in Eq. (S20). However, we also compute the instantaneous distance d between the centroid of the electron and the GDS, for each snapshot from the simulations. Since the vapor phase should have a dielectric of $\epsilon_{\mathrm{vac}} = 1$, we use a similar hyperbolic tangent function to interpolate $\epsilon(z)$ across the GDS:

$$\epsilon(z) = \frac{1}{2}\Big[\epsilon_{\mathrm{static}} + \epsilon_{\mathrm{vac}} + (\epsilon_{\mathrm{vac}} - \epsilon_{\mathrm{static}})\tanh\Big(\alpha|z-d|\Big)\Big] \,. \tag{S21}$$

Here, $z = 0$ defines the middle of the slab, so Eq. (S21) corresponds to a midpoint of $z = d$ for the switching function at the water/vapor interface. A diagram of this interfacial setup appears in Fig. S7.

3.2.4 Non-Equilibrium Poisson Formalism

To compute the solvation free energy due to the solvent polarization response arising from vertical detachment of an electron in an anionic system, we follow the non-equilibrium solvation formalism presented in Refs. S50 and S51, adapting it from the two-dimensional surface approach that is appropriate for apparent surface charge PCMs to the three-dimensional approach that is required here. Within this methodology, two separate SCF calculations are required. The first one generates the electrostatic potentials and solvation free energies of the reference state, which we denote as "0", and the second generates the necessary quantities for the final state, "1". In the interest of generality, we will refer to the latter as the

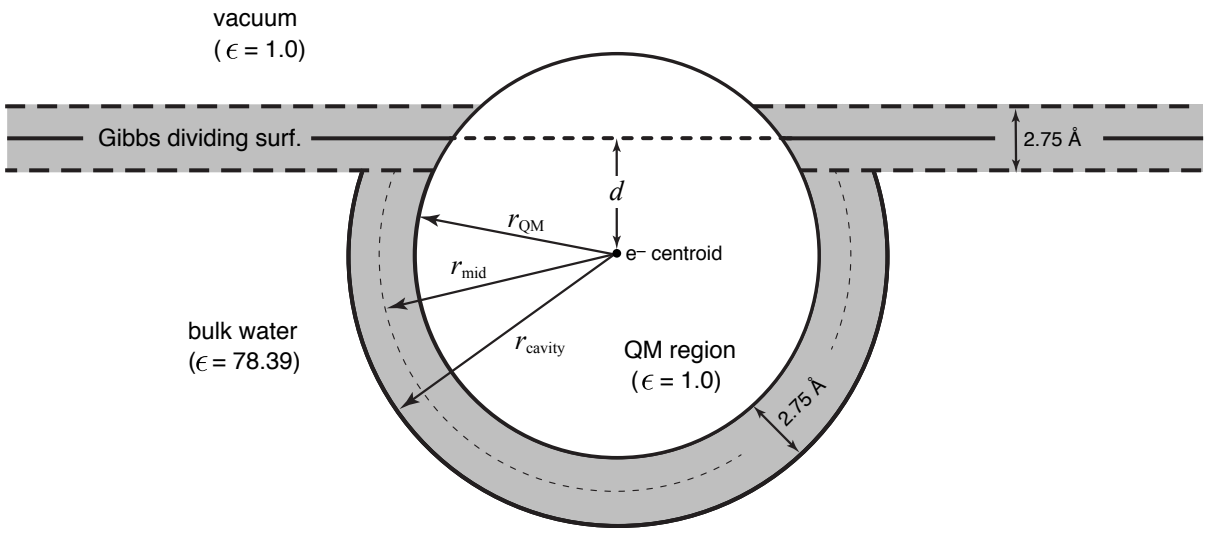

Figure S7: Diagram of the setup for the QM/Poisson calculations at the water/vacuum interface. Within the two shaded regions, the dielectric function is interpolated between $\epsilon = 1.0$ and $\epsilon = 78.39$, as described in the text. The interfacial region around the GDS uses the switching function in Eq. (S21), whereas the spherical cavity in bulk water uses the same switching function used for bulk solvation, Eq. (S20).

"ionized" state, but bear in mind that for the present application the reference state is an anionic water cluster so the "ionized" state is actually a neutral water cluster.

The free energy G_0 of the (anionic) reference system is computed in the usual way:[S50,S51]

$$G_0 = E_{\text{solute},0} + \tfrac{1}{2} \int d\mathbf{r}\; \varphi_{\text{pol},0}(\mathbf{r})\; \rho_{\text{solute},0}(\mathbf{r})\;. \tag{S22}$$

The "0" subscripts indicate that the quantities in question arise from the reference state; later we will require similar quantities for the final state. All of the necessary terms in Eq. (S22) can be obtained from the QM/Poisson algorithm presented in Section 3.2.2. The energies, electrostatic potentials, and charge densities of the reference state are stored in core memory to be used in the second calculation, for the ionized final state "1".

Once the first SCF calculation is complete for the anionic reference state, the second calculation begins for the ionized state. We have chosen to adapt the first-order perturbative correction scheme for non-equilibrium PCM[S50,S51] for use with our Poisson equation solver. Although originally presented in the context of polarizable continuum solvation effects on vertical *excitation* energies, it is noted in Refs. S50 and S51 that the formalism is equally valid for vertical *ionization*. The algorithm outlined in Section 3.2.2 requires a few minor adjustments for the non-equilibrium case, as discussed below.

Within the first-order perturbative approximation, the effective Hamiltonian for the ionized state is given by[S50]

$$\hat{H}_1 = \hat{H}_{\text{vac}} + \hat{V}^{\text{slow}}_{\text{pol},0} + \hat{V}^{\text{fast}}_{\text{pol},0} + \lambda \left(\hat{V}^{\text{fast}}_{\text{pol},1} - \hat{V}^{\text{fast}}_{\text{pol},0} \right), \tag{S23}$$

where $\hat{H}_{\text{vac}}$ is the vacuum Hamiltonian (Kohn-Sham operator) for the ionized solute and the

operator $\hat{V}_{\mathrm{pol},k}$ ($k = 0$ or 1) generates the polarization potential $\varphi_{\mathrm{pol},k}(\mathbf{r})$ due to the dielectric response. The superscripts "slow" and "fast" reflect which component of the polarization charge density we are using to construct the potential; see discussions in Section 3.1 and below. The quantity λ is the usual perturbation parameter.

For the ionized final state, two modifications of the equilibrium QM/Poisson algorithm presented above are required in the non-equilibrium case. First, the total free energy is computed differently due to the first-order perturbative correction, and second, the Fock matrix correction [Eq. (S19)] must use the reference state polarization potential as opposed to using the polarization potential arising from the ionized state.[S50,S51] The first-order energy correction $E^{(1)}$, specifically for the ionized state, is

$$E_1^{(1)} = \int d\mathbf{r}\; \varphi_{\mathrm{solute},1}(\mathbf{r}) \left[\rho_{\mathrm{pol},1}^{\mathrm{fast}}(\mathbf{r}) - \rho_{\mathrm{pol},0}^{\mathrm{fast}}(\mathbf{r})\right] \;, \tag{S24}$$

where the term in square brackets is the difference between the fast components of the ionized- and reference-state densities. We use the Marcus partition[S51,S70–S73] to separate the polarization charge densities into fast and slow contributions. This amounts to

$$\rho_{\mathrm{pol},k}(\mathbf{r}) = \rho_{\mathrm{pol},k}^{\mathrm{slow}}(\mathbf{r}) + \rho_{\mathrm{pol},k}^{\mathrm{fast}}(\mathbf{r}) \tag{S25}$$

$$\rho_{\mathrm{pol},k}^{\mathrm{slow}}(\mathbf{r}) = (\chi_{\mathrm{slow}}/\chi_{\mathrm{e}})\, \rho_{\mathrm{pol},k}(\mathbf{r}) \tag{S26}$$

$$\frac{\chi_{\mathrm{slow}}}{\chi_{\mathrm{e}}} = \frac{\epsilon_{\mathrm{static}} - \epsilon_\infty}{\epsilon_{\mathrm{static}} - 1} \;. \tag{S27}$$

(Consult Ref. S51 for a discussion of the Marcus partition versus the Pekar partition in the context of non-equilibrium dielectric continuum solvation. Solvation energies are nearly identical between the two models, although the interpretation of fast versus slow charge is different, but this is of no consequence here.)

The dielectric constants on the right side of Eq. (S27) are the same as those discussed in Section 3.1, thus the requisite fast and slow components of the polarization potentials can be found using Eqs. (S25)–(S27), then using the definition of the electrostatic potential to obtain

$$\varphi_{\mathrm{pol},k}(\mathbf{r}) = \int d\mathbf{r}'\; \frac{\rho_{\mathrm{pol},k}(\mathbf{r}')}{|\mathbf{r} - \mathbf{r}'|} \;. \tag{S28}$$

It should be noted that employing Eqs. (S20) and (S21) to create spatially-varying dielectric functions in Eq. (S27) is unnecessary; the component of the smoothing functions containing the spatial dependence algebraically cancels out, and thus the ratio $\chi_{\mathrm{slow}}/\chi_{\mathrm{e}}$ is constant across the grid. The spatially-varying nature of the dielectric is carried solely by the static dielectric function used to compute the polarization charge in Eq. (S13) and iterative charge densities in Eqs. (S14) and (S15).

Next we discuss the first-order polarization energy within the perturbative scheme as well as an additional correction that must be included due to our choice of the Marcus partition. The first-order polarization energy correction term is

$$W_1^{(1)} = \tfrac{1}{2} \int d\mathbf{r}\; \varphi_{\mathrm{solute},1}(\mathbf{r}) \left[\rho_{\mathrm{pol},1}^{\mathrm{fast}}(\mathbf{r}) - \rho_{\mathrm{pol},0}^{\mathrm{fast}}(\mathbf{r})\right] - W_{0,1} \;, \tag{S29}$$

Algorithm 2: Non-Equilibrium QM/Poisson SCF Procedure

begin Reference State Calculation
  Use Algorithm 1 to compute the energies, electrostatic potentials, and charge densities for the solvated reference state and save to disk.
Input: G_0, $\varphi_{\mathrm{pol},0}$, and $\rho_{\mathrm{tot},0}$ for the reference state.
begin Final State Procedure
  Initialize $\Delta\mathbf{F} \equiv 0$.
  repeat $n = 1, 2, \ldots$ SCF iterations
    Diagonalize the Fock matrix $\mathbf{F} = \mathbf{F}_0 + \Delta\mathbf{F}$ to obtain the density matrix $\mathbf{P}^{(n)}$, where $\mathbf{F}_0$ is the gas-phase Fock matrix and $\Delta\mathbf{F}$ is the solvation correction.
    Compute the electronic and nuclear charge densities at each grid point using Eqs. (S9) and (S10), and the solute charge density using Eq. (S8).
    begin Finite-difference Poisson solver
      Use the conjugate gradient Poisson solver (adapted from Ref. S65) to compute $\varphi_{\mathrm{solute},1}(\mathbf{r})$ with $\epsilon(\mathbf{r}) \equiv 1$.
    Use $\varphi_{\mathrm{solute},1}(\mathbf{r})$ to form $\rho_{\mathrm{iter},1}(\mathbf{r})$ and update $\rho_{\mathrm{tot},1}(\mathbf{r})$.
    repeat $i = 1, 2, \ldots$ Poisson solver iterations
      begin Electrostatic potential solver
        Compute $\varphi^{(i)}_{\mathrm{tot},1}(\mathbf{r})$ using Eq. (S12) and dielectric function $\epsilon(\mathbf{r})$.
        `// The form of the dielectric function is discussed in Section 3.2.3.`
      Use $\varphi^{(i)}_{\mathrm{iter},1}$ to form the updated density $\rho^{(i+1)}_{\mathrm{iter},1}$ [Eq. (S15)]. Also update $\rho_{\mathrm{pol},1}$ [Eq. (S13)] and $\rho_{\mathrm{tot},1}$ [Eq. (S7)].
    until $||\rho^{(i+1)}_{\mathrm{iter},1}(\mathbf{r}) - \rho^{(i)}_{\mathrm{iter},1}(\mathbf{r})|| < 10^{-5}$ a.u.
    Compute $\varphi_{\mathrm{pol},1} = \varphi_{\mathrm{tot},1} - \varphi_{\mathrm{solute},1}$.
    Generate the Fock matrix correction in Eq. (S19) using the *reference* state polarization potential, $\varphi_{\mathrm{pol},0}$.
    Compute the final-state polarization free energy G_1 using Eq. (S31) and add it to the SCF energy
  until *DIIS error* $< 10^{-5}$ a.u.
  Compute VEBE $= G_1 - G_0$

where the first term is half of the first-order energy correction and the second corrects for the Coulomb interaction between the slow and fast polarization charges. (Physically, this describes a situation in which the slow component of the reference-state polarization affects the fast polarization from the ionized state.[S51,S59,S70,S74]) The final term in Eq. (S29) is

$$W_{0,1} = \tfrac{1}{2} \int d\mathbf{r}\; \varphi^{\text{slow}}_{\text{pol},0}(\mathbf{r}) \left[\rho^{\text{fast}}_{\text{pol},1}(\mathbf{r}) - \rho^{\text{fast}}_{\text{pol},0}(\mathbf{r}) \right] \; . \tag{S30}$$

The total solvation free energy for the ionized state can now be computed according to

$$G_1 = E_{\text{solute},1} + \tfrac{1}{2} \int d\mathbf{r}\; \varphi_{\text{pol},0}(\mathbf{r})\; \rho_{\text{solute},1}(\mathbf{r}) + E_1^{(1)} - W_1^{(1)} \; . \tag{S31}$$

Note that the integral on the right is identical to that in Eq. (S22) because the same anionic reference-state polarization potential is used to update the Fock matrix for both SCF calculations.[S51] An outline of the non-equilibrium QM/Poisson procedure is presented as Algorithm 2 on pg. S23.

References

(S1) Turi, L.; Borgis, D. *J. Chem. Phys.* **2002**, *117*, 6186–6195.

(S2) Berendsen, H. J. C.; Postma, J. P. M.; van Gunsteren, W. F.; Hermans, J. . In *Intermolecular Forces*; Pullman, B., Ed.; Dordrecht: Holland, 1981.

(S3) Jacobson, L. D.; Herbert, J. M. *J. Chem. Phys.* **2010**, *133*, 154106:1–19.

(S4) Ren, P.; Ponder, J. W. *J. Phys. Chem. B* **2003**, *107*, 5933–5947.

(S5) Jacobson, L. D.; Williams, C. F.; Herbert, J. M. *J. Chem. Phys.* **2009**, *130*, 124115:1–18.

(S6) Turi, L.; Sheu, W.-S.; Rossky, P. J. *Science* **2005**, *309*, 914–917.

(S7) Turi, L.; Madarász, Á.; Rossky, P. J. *J. Chem. Phys.* **2006**, *125*, 014308:1–7.

(S8) Borgis, D.; Rossky, P. J.; Turi, L. *J. Chem. Phys.* **2006**, *125*, 064501:1–13.

(S9) Borgis, D.; Rossky, P. J.; Turi, L. *J. Chem. Phys.* **2007**, *127*, 174508:1–6.

(S10) Madarász, Á.; Rossky, P. J.; Turi, L. *J. Chem. Phys.* **2007**, *126*, 234707:1–11.

(S11) Madarász, A.; Rossky, P. J.; Turi, L. *J. Chem. Phys.* **2009**, *130*, 124319:1–7.

(S12) Tay, K. A.; Boutin, A. *J. Phys. Chem. B* **2009**, *113*, 11943–11949.

(S13) Jacobson, L. D.; Herbert, J. M. *J. Am. Chem. Soc.* **2010**, *132*, 10000–10002.

(S14) Jacobson, L. D.; Herbert, J. M. *Science* **2011**, *331*, 1387.

(S15) Jacobson, L. D.; Herbert, J. M. *J. Chem. Theory Comput.* **2011**, *7*, 2085–2093.

(S16) Jacobson, L. D.; Herbert, J. M. *J. Am. Chem. Soc.* **2011**, *133*, 19889–19899.

(S17) Herbert, J. M.; Jacobson, L. D. *J. Phys. Chem. A* **2011**, *115*, 14470–14483.

(S18) Glover, W.; Casey, J. R.; Schwartz, B. J. *J. Chem. Theory Comput.* **2014**, *10*, 4661–4671.

(S19) Casey, J. R.; Schwartz, B. J.; Glover, W. J. *J. Phys. Chem. Lett.* **2016**, *7*, 3192–3198.

(S20) Smith, E. R. *Proc. R. Soc. London A* **1981**, *375*, 475–505.

(S21) Yeh, I.-C.; Berkowitz, M. L. *J. Chem. Phys.* **1999**, *111*, 3155–3162.

(S22) Becke, A. D. *Phys. Rev. A* **1988**, *38*, 3098–3100.

(S23) Tsuneda, T.; Suzumura, T.; Hirao, K. *J. Chem. Phys.* **2008**, *110*, 10664–10678.

(S24) Lee, C.; Yang, W.; Parr, R. G. *Phys. Rev. B* **1988**, *37*, 785–789.

(S25) Rohrdanz, M. A.; Herbert, J. M. *J. Chem. Phys.* **2008**, *129*, 034107:1–9.

(S26) Rohrdanz, M. A.; Martins, K. M.; Herbert, J. M. *J. Chem. Phys.* **2009**, *130*, 054112:1–8.

(S27) Shao, Y. *et al. Mol. Phys.* **2015**, *113*, 184–215.

(S28) Richard, R. M.; Herbert, J. M. *J. Chem. Theory Comput.* **2011**, *7*, 1296–1306.

(S29) Yagi, K.; Okano, Y.; Sato, T.; Kawashima, Y.; Tsuneda, T.; Hirao, K. *J. Phys. Chem. A* **2008**, *112*, 9845–9853.

(S30) Baer, R.; Livshits, E.; Salzner, U. *Annu. Rev. Phys. Chem.* **2010**, *61*, 85–109.

(S31) Herbert, J. M. The quantum chemistry of loosely bound electrons. In *Reviews in Computational Chemistry*, Vol. 28; Parill, A. L.; Lipkowitz, K., Eds.; Wiley-VCH: 2015.

(S32) Wong, B. M.; Hsieh, T. H. *J. Chem. Theory Comput.* **2010**, *6*, 3704–3712.

(S33) Uhlig, F.; Herbert, J. M.; Coons, M. P.; Jungwirth, P. *J. Phys. Chem. A* **2014**, *118*, 7507–7515.

(S34) Garrett, K.; Vazquez, X. A. S.; Egri, S. B.; Wilmer, J.; Johnson, L. E.; Robinson, B. H.; Isborn, C. M. *J. Chem. Theory Comput.* **2014**, *10*, 3821–3831.

(S35) Uhlig, F.; Marsalek, O.; Jungwirth, P. *J. Phys. Chem. Lett.* **2012**, *3*, 3071–3075.

(S36) Uhlig, F.; Marsalek, O.; Jungwirth, P. *J. Phys. Chem. Lett.* **2013**, *4*, 338–343.

(S37) Herbert, J. M.; Head-Gordon, M. *J. Phys. Chem. A* **2005**, *109*, 5217–5229.

(S38) Herbert, J. M.; Head-Gordon, M. *Phys. Chem. Chem. Phys.* **2006**, *8*, 68–78.

(S39) Williams, C. F.; Herbert, J. M. *J. Phys. Chem. A* **2008**, *112*, 6171–6178.

(S40) Willard, A. P.; Chandler, D. *J. Phys. Chem. B* **2010**, *110*, 1954–1958.

(S41) Turi, L. *J. Chem. Phys.* **2016**, *144*, 154311-1:9.

(S42) Siefermann, K. R.; Liu, Y.; Lugovoy, E.; Link, O.; Faubel, M.; Buck, U.; Winter, B.; Abel, B. *Nat. Chem.* **2010**, *2*, 274–279.

(S43) Tang, Y.; Shen, H.; Sekiguchi, K.; Kurahashi, N.; Mizuno, T.; Suzuki, Y. I.; Suzuki, T. *Phys. Chem. Chem. Phys.* **2010**, *12*, 3653–3655.

(S44) Shreve, A. T.; Yen, T. A.; Neumark, D. M. *Chem. Phys. Lett.* **2010**, *493*, 216–219.

(S45) Buchner, F.; Schultz, T.; Lübcke, A. *Phys. Chem. Chem. Phys.* **2012**, *14*, 5837–5842.

(S46) Coe, J. V.; Williams, S. M.; Bowen, K. H. *Int. Rev. Phys. Chem.* **2008**, *27*, 27–51.

(S47) Tomasi, J.; Mennucci, B.; Cammi, R. *Chem. Rev.* **2005**, *105*, 2999–3093.

(S48) Herbert, J. M.; Lange, A. W. Polarizable continuum models for (bio)molecular electrostatics: Basic theory and recent developments for macromolecules and simulations. In *Many-Body Effects and Electrostatics in Biomolecules*; Cui, Q.; Ren, P.; Meuwly, M., Eds.; Pan Stanford: 2016.

(S49) Fisicaro, G.; Genovese, L.; Andreussi, O.; Marzari, N.; Goedecker, S. *J. Chem. Phys.* **2016**, *144*, 014103:1–12.

(S50) Mewes, J.-M.; You, Z.-Q.; Wormit, M.; Kriesche, T.; Herbert, J. M.; Dreuw, A. *J. Phys. Chem. A* **2015**, *119*, 5446–5464.

(S51) You, Z.-Q.; Mewes, J.-M.; Dreuw, A.; Herbert, J. M. *J. Chem. Phys.* **2015**, *143*, 234107:1–10.

(S52) Cancès, E.; Mennucci, B. *J. Chem. Phys.* **2001**, *114*, 4744–4745.

(S53) Chipman, D. M. *Theor. Chem. Acc.* **2002**, *107*, 80–89.

(S54) Lange, A. W.; Herbert, J. M. *Chem. Phys. Lett.* **2011**, *509*, 77–87.

(S55) Cramer, C. J.; Truhlar, D. G. *Acc. Chem. Res.* **2008**, *41*, 760–768.

(S56) Klamt, A.; Mennucci, B.; Tomasi, J.; Barone, V.; Curutchet, C.; Orozco, M.; Luque, F. J. *Acc. Chem. Res.* **2009**, *42*, 489–492.

(S57) Pomogaeva, A.; Chipman, D. M. *J. Chem. Theory Comput.* **2014**, *10*, 211–219.

(S58) Tomasi, J.; Persico, M. *Chem. Rev.* **1994**, *94*, 2027–2094.

(S59) Cammi, R.; Tomasi, J. *Int. J. Quantum Chem. Symp.* **1995**, *29*, 465–474.

(S60) Cossi, M.; Barone, V. *J. Phys. Chem. A* **2000**, *104*, 10614–10622.

(S61) Improta, R.; Barone, V.; Scalmani, G.; Frisch, M. J. *J. Chem. Phys.* **2006**, *125*, 054103:1–9.

(S62) Zhang, Y.; Xu, Z. *Amer. Miner.* **1995**, *80*, 670–675.

(S63) Chipman, D. M. *J. Chem. Phys.* **1999**, *110*, 8012–8018.

(S64) Chipman, D. M. *J. Chem. Phys.* **2000**, *112*, 5558–5565.

(S65) Wang, J.; Luo, R. *J. Comput. Chem.* **2010**, *31*, 1689–1698.

(S66) Lange, A. W.; Herbert, J. M. *J. Chem. Phys.* **2010**, *133*, 244111:1–18.

(S67) Andreussi, O.; Dabo, I.; Marzari, N. *J. Chem. Phys.* **2012**, *136*, 064102:1–20.

(S68) Davis, M. E.; McCammon, J. A. *J. Comput. Chem.* **1991**, *12*, 909–912.

(S69) Grant, J. A.; Pickup, B. T.; Nicholls, A. *J. Comput. Chem.* **2001**, *22*, 608–640.

(S70) Marcus, R. A. *J. Chem. Phys.* **1956**, *24*, 966–978.

(S71) Marcus, R. A. *J. Chem. Phys.* **1956**, *24*, 979–989.

(S72) Brady, J. E.; Carr, P. W. *J. Phys. Chem.* **1985**, *89*, 5759–5766.

(S73) Klamt, A. *J. Phys. Chem.* **1996**, *100*, 3349–3353.

(S74) Aguilar, M. A.; Olivares del Valle, F. J.; Tomasi, J. *J. Chem. Phys.* **1993**, *98*, 7375–7384.